Article

Not peer-reviewed version

Photoelectrochemical Biosensor Based On 1D $ZnIn_2S_4$ Nanosheet Decorated 2D In_2O_3 Tube For Sensitive PSA Detection

Huihui Shi , Jianjian Xu , Yanhu Wang *

Posted Date: 24 March 2025

doi: 10.20944/preprints202503.1745.v1

Keywords: photoelectrochemical; In_2O_3-$ZnIn_2S_4$; hetero-interfaces; charge separation; PSA

 doi:10.20944/preprints202503.1745.v1

Article

Photoelectrochemical Biosensor Based On 1D $ZnIn_2S_4$ Nanosheet Decorated 2D In_2O_3 Tube For Sensitive PSA Detection

Huihui Shi [1,2], Jianjian Xu [3] and Yanhu Wang [2,*]

[1] Key Lab of MEMS of Ministry of Education, Southeast University, Nanjing 210096, China
[2] Shandong Analysis and Test Center, Qilu University of Technology (Shandong Academy of Sciences), Jinan 250014, China
[3] Department of Food and Drug, Weihai Ocean Vocational College, Weihai 264300, China
* Correspondence: wyhloving633@163.com

Abstract: In photoelectrochemical biosensing, efficient electron-hole separation is crucial to obtain preferred photocurrent response and analytical performance; thus, constructing developed heterointerfaces with high carriers transfer efficiency is an effective way for sensitive evaluation of analytes. Herein, 1D $ZnIn_2S_4$ nanosheet decorated 2D In_2O_3 tube was developed to integrate with prostate antigen (PSA)-sensitive aptamer for PSA sensitive detection. Benefiting from photoelectric effect and specific 1D/2D hierarchical structure, In_2O_3-$ZnIn_2S_4$ displayed enhanced optical absorption and photocarrier separation, thus superior photoelectrochemical response. Proposed bioassay protocol possessed the linear range from 0.001 to 50 ng/mL and a detection limit at 0.00037 ng/mL. In addition, this biosensor exhibited satisfy anti-interface ability and stability, which also could be extended to other quantitative platforms for detecting else proteins.

Keywords: photoelectrochemical; In_2O_3-$ZnIn_2S_4$; hetero-interfaces; charge separation; PSA

1. Introduction

Photoelectrochemical (PEC) bioanalysis, featuring high sensitivity and simple equipment, has been used to quantify various analytes through photocurrent variation [1,2]. Essentially, sensing signals strongly depend on light-electricity conversion process and carrier separation efficiency of photoactive materials. Thus, besides recognition units, photoactive materials with superior PEC performance are crucial factors when designing sensitive PEC biosensors. Indium oxide (In_2O_3), a typical moderate-band-gap n-type semiconductor, has been widely used in photoelectrochemistry due to its high chemical stability, low resistivity, low toxicity, and easy preparation [3,4]. However, pure In_2O_3 suffered from poor PEC performance, which was mainly contributed to high carrier rate, limited photon utilization, and deficient surface active sites. Multiple reports have been demonstrated heterojunction construction by coupling else semiconductor with different band gaps could prominently enhance PEC performance of In_2O_3-based materials [5–8].

Up to now, multiple In2O3-based heterostructures, such as In_2O_3/Co_3O_4 [9], In_2O_3/g-C_3N_4 [10], In_2O_3/CdS [11], and In_2O_3/In_2S_3 [12], have been prepared with improved photoelectric transformation efficiency. However, mismatched lattice between these semiconductors and In_2O_3 usually increase heterointerface impedance and restrict carriers separation. Compared with above mentioned semiconductors, 2D layered $ZnIn_2S_4$ has drawn increasing attention due to short carrier migration pathways, rich active sites, and similar lattice parameters [13,14]. High lattice matching degree of In_2O_3 and $ZnIn_2S_4$ is conducive to the formation of compact interface and thus greatly decreases charge immigration impedance of the heterointerface, and finally facilitates spatial charge separation [15]. A significant challenge is that $ZnIn_2S_4$ sheets tend to agglomerate into nanoclusters, causing low specific surface area and reduced active sites [16,17]. Supporting carriers including CdS nanocube,

 doi:10.20944/preprints202503.1745.v1

NiMoOx nanorod, $FeWO_4$ flower, and Co_9S_8 tube, favor lamellar growth and inhibit agglomerate [18–21]. Thus, it is of great favor to employ 1D In_2O_3 as the supporter to offer abundant area for nanosheet growth and conduction paths for photogenerated carrier transport. With such design, branched $ZnIn_2S_4$ nanosheets on In_2O_3 tubes could facilitate solar-light harvesting and intimate heterointerface could modulate the migration pathway for extending the photogenerated charge lifetime.

In this work, a 1D/2D heterostructure was designed by decorating ZnIn2S4 nanosheets onto In_2O_3 tubes to integrate with the prostate antigen (PSA)-sensitive aptamer for PSA quantification. The overall heterostructure preparation process involved template method and in-situ growth strategy where MIL-68 was transformed into tubular In_2O_3 and further modification of $ZnIn_2S_4$ nanosheets (Figure 1A). Under visible light, nanosized heterogeneous interface favored the effective separation and migration of electron-hole pairs, endowing hybrid with desirable PEC performance (Figure 1B). Furthermore, modified aptamer on the PEC electrodes could specifically binding with target, thus a relevance between PSA concentration and photocurrent response was established. Such simple and efficient sensing protocol has great potential in other biomolecule quantification.

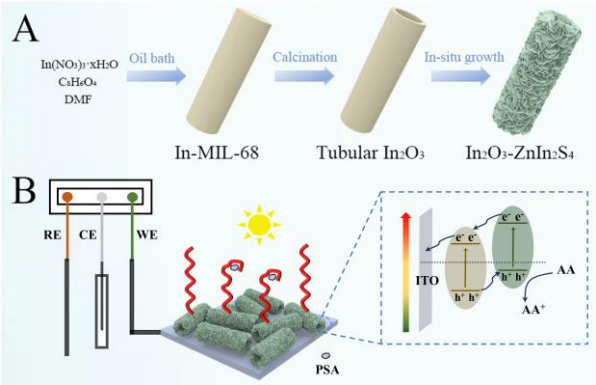

Figure 1. (A) Schematic illustration of In_2O_3-$ZnIn_2S_4$ synthesize route. (B) Schematic illustration of PEC electrode and sensing mechanism.

2. Materials and Methods

2.1. Preparation of Hollow Tubular In_2O_3

Tubular In_2O_3 was synthesized by sequential hydrothermal and thermal methods. Initially, indium nitrate hydrate (0.06 g) and 1,4-benzenedicarboxylic acid (0.06 g) were dissolved in 40 mL N,N-dimethylformamide, and further stirred for 5 min at room temperature. Resultant solution was heated at 120 °C for 30 min, followed by filtrated and washed with ethanol to obtain white MIL-68. Finally, an annealing procedure at 500 °C was performed for 2 h in a muffle furnace, yielding light yellow In_2O_3 tubes.

2.2. Synthesis of Branched Sheet Embedded Tubular In_2O_3-$ZnIn_2S_4$

Briefly, as-prepared In_2O_3 tubes (0.1 g) and $ZnIn_2S_4$ precursor (0.05 g of zinc chloride, 0.23 g indium chloride, and 0.24 g thioacetamide) were fully dissolved in 30 mL deionized water and then stirred continuously for 30 min at 80 °C in an oil bath. The obtained precipitate In_2O_3-$ZnIn_2S_4$ was collected, centrifugated, washed with deionized water, and dried under vacuum. Nanosheet-based $ZnIn_2S_4$ clusters were synthesized using the same method without the addition of In_2O_3.

2.3. Fabrication of Sensing Platform and Analysis Protocol

FTO glass was pre cleaned sequentially with acetone, ethanol, and deionized water under violent ultrasonication. In order to obtain an attractive PEC signal, 1 mL prepared In_2O_3-$ZnIn_2S_4$ solution was spin-coated onto the FTO glass, followed by drying under an infrared lamp for 30 min. 50 μL chitosan aqueous solution (0.08 wt%) in 1% acetic acid was dropped onto FTO electrode and

 doi:10.20944/preprints202503.1745.v1

then 5 wt% glutaraldehyde solution was applied onto the electrode to trigger amino groups for subsequent biomolecule modification. After that, the electrode was dealt with 20 μL 1 μM aptamer for 70 min at 4℃, followed by the addition of 10 μL of 2wt% bovine serum albumin (BSA) to block non-specific binding sites. Obtained working electrode was stored at 4℃ and denoted as FTO/In_2O_3-$ZnIn_2S_4$/aptamer/BSA. Before PEC measurements, FTO/In_2O_3-$ZnIn_2S_4$/aptamer/BSA was incubated with 20 μL PSA at room temperature for 30 min. Notably, FTO electrodes were thoroughly cleaned by PBS buffer (pH=7.4, 0.01 M) after each step. All PEC signals were generated by a typical three-electrode system (FTO working electrode, counter electrode and reference electrode) in 0.1 M ascorbic acid (AA) solution.

2.4. Detection Limit Calculation

Detection limit was obtained by the formula $I_{LOD}=I_{blank}+3S_{blank}$, where I_{blank} and S_{blank} are average photocurrent of 10 independent samples (without PSA) and corresponding standard deviation, respectively. Then, I_{LOD} was brought into the regression curve to obtain detection limit.

3. Results and Discussion

3.1. Morphology and Structure Characterization

Hybrid In_2O_3-$ZnIn_2S_4$ was synthesized by template method and in-situ growth technique, and further investigated by scanning electron microscope (SEM), transmission electron microscope (TEM), and high-resolution TEM (HRTEM). Apparently, a highly dispersed tube microstructure with well-defined tube walls and cavities was found for In_2O_3 (Figure 2A), providing adequate space for $ZnIn_2S_4$ growth. While pure $ZnIn_2S_4$ displayed irregular clusters assembled by a large amount of nanosheets (Figure 2B and Figure S1). After loading nanosheets onto In_2O_3, as-prepared composite exhibited uniform and dense coverage of ultrathin nanosheets, and O, In, S, and Zn elements were evenly distributed on the single tube (Figure 2C and D). Significantly, compared self-assembled $ZnIn_2S_4$ nanosheet clusters, interconnected nanosheets is beneficial for increasing specific surface area and providing sufficient active sites. Furthermore, a tight interfacial junction between In_2O_3 and $ZnIn_2S_4$ was successfully constructed where lattice spacing of 0.29 and 0.32 nm were ascribed to the In_2O_3 (2 2 2) and $ZnIn_2S_4$ (1 0 2) crystal planes, respectively (Figure 2E) [22]. These images demonstrated the successful fabrication of branched sheet embedded tubular hybrid and heterostructure.

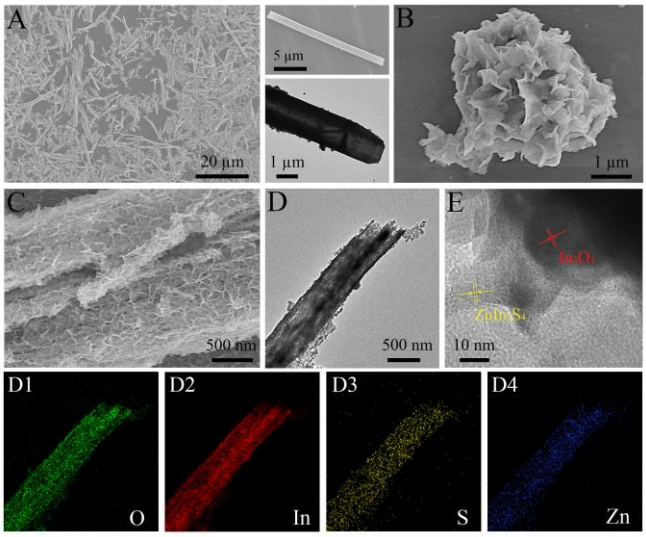

Figure 2. (A) SEM images of (A) pure In_2O_3, (B) pure $ZnIn_2S_4$, and (C) In_2O_3-$ZnIn_2S_4$. (D) TEM image, elemental mappings and (E) HRTEM image of In_2O_3-$ZnIn_2S_4$.

 doi:10.20944/preprints202503.1745.v1

Optical properties, crystalline phases, and chemical states were also measured by UV-vis absorption spectra, X-ray diffraction (XRD), and X-ray photoelectron spectroscopy, respectively. As shown in Figure 3A, a typical absorption edge at ~425 nm and poor light-harvesting capacity in visible light region were demonstrated for pure In_2O_3. For hybrid In_2O_3-$ZnIn_2S_4$, a robust photo-absorption in UV and visible light region to ~542 nm was obtained. Using Tauc plots method [23], the bandgap energies (Eg) of In_2O_3, $ZnIn_2S_4$, In_2O_3-$ZnIn_2S_4$ were calculated to be 2.9, 2.58, and 2.29 eV, respectively. Furthermore, XRD patterns of above materials were shown in Figure 3B. Nine distinct diffraction peaks at 21.5°, 30.6°, 35.5°, 37.7°, 41.8°, 43.7°, 51.1°, 55.9°, 60.7° in black curve were well-matched with characteristic standard In_2O_3 data (JCPDS No. 06-0416) [24]. Except diffraction peaks of In_2O_3, additional peak at 47.2° gathered from In_2O_3-$ZnIn_2S_4$ was assigned to (1 1 0) crystal plane of pure $ZnIn_2S_4$. To probe the elemental valence details, X-ray photoelectron spectroscopy (XPS) was performed with C 1s peak as the standard reference. In the survey spectrum, the presence of In, O, Zn, and S elements was confirmed, consistent with above mentioned mapping diagram. In specific, two binding energies at 1022.3 and 1045.5 eV were attributed to Zn 2p3/2 and Zn 2p1/2 of Zn^{2+} chemical state. Two prominent peaks presented at 445.2 eV (In 3d5/2) and 452.8 eV (In 3d3/2) were recorded, which were similar to that of standard In^{3+}. S 2p spectrum could be deconvoluted into two characteristic S^{2-} peaks at 161.8 and 163.0 eV. In a word, above mentioned results matched each other, illustrating the successful fabrication of tubular In_2O_3-$ZnIn_2S_4$.

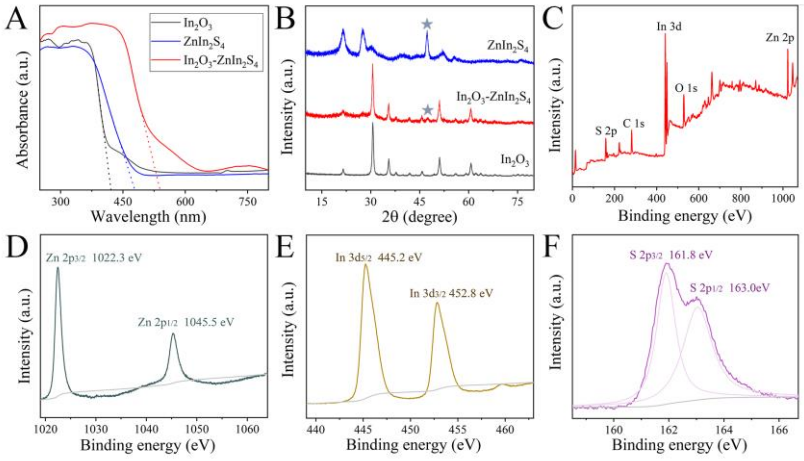

Figure 3. (A) UV-vis absorption spectra and (B) XRD patterns of In_2O_3, $ZnIn_2S_4$, and In_2O_3-$ZnIn_2S_4$. High-resolution XPS spectra of (C) In_2O_3-$ZnIn_2S_4$, (D)Zn 2p, (E)In 3d, and (F) S 2p.

3.2. PEC and EIS Behaviors

Stepwise modification process of PSA sensing platform was estimated by electrochemical impedance spectroscopy (EIS) where the larger radius always means lower charge transfer rate (Figure 4A). It could be observed that the electron-transfer resistance (Ret) elevated dramatically after immobilization of In_2O_3-$ZnIn_2S_4$ complex onto the FTO surface due to their low conductivity. With the identify element and blocking agent modification progress, Ret witnessed an upward trend. This is because large steric hindrance of aptamer and BSA diminished charge transfer capacity. Moreover, the transient photocurrent responses were also measured using 0.1 M ascorbic acid solution as the sacrificial agent (Figure 4B). As expected, FTO/In_2O_3-$ZnIn_2S_4$ (red curve) showed a significant photocurrent enhancement compared with FTO/In_2O_3 (black curve) thanks to the heterointerfaces promoting photogenerated electron-hole separation. Under visible light radiation, photoinduced electrons and holes were generated on the In_2O_3 and $ZnIn_2S_4$ surface. Driven by the internal electric field, photoinduced electrons and holes were accumulated on the conduction band of $ZnIn_2S_4$ and valance band of In_2O_3, respectively. An enhanced anodic photocurrent was obtained and holes were captured by electron donor (ascorbic acid). After photoelectrode incubated with non-conductive

 doi:10.20944/preprints202503.1745.v1

aptamer and BSA, the continuously decreasing photocurrent value was obtained (blue and green curves). EIS and PEC response demonstrated continuous fixation of biomolecules on the FTO electrode.

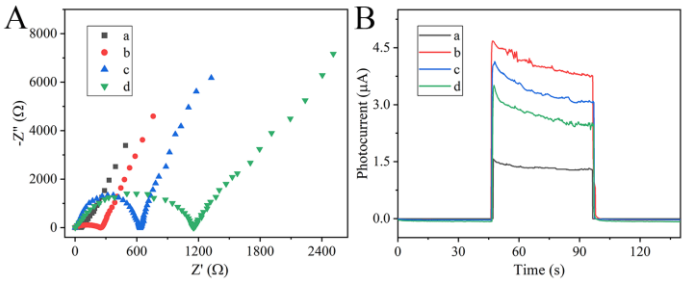

Figure 4. (A) EIS spectra of (a) FTO, (b) FTO/In_2O_3-$ZnIn_2S_4$, (c) FTO/In_2O_3-$ZnIn_2S_4$/aptamer, and (d) FTO/In_2O_3-$ZnIn_2S_4$/aptamer/BSA in 5.0 mM $[Fe(CN)_6]^{3-/4-}$ containing 0.1 M potassium chloride. (B) Photocurrent responses of (a) FTO, (b) FTO/In_2O_3-$ZnIn_2S_4$, (c) FTO/In_2O_3-$ZnIn_2S_4$/aptamer, and (d) FTO/In_2O_3-$ZnIn_2S_4$/aptamer/BSA in 0.1 M ascorbic acid solution.

3.3. Analytical Performance

PSA level, as an early portent of prostate dysfunction, is associated with prostate cancer, underscoring the importance of sensitive PSA detection. Thus, based on this well-designed PEC biosensor, we further explored its capability for the quantification of PSA antigen. According to analysis protocol mentioned in experimental section, PSA at different concentrations was applied onto photoelectrodes and acquired PEC signals were analyzed. After incubation with 0.001 ng/mL PSA, the photocurrent intensity abated (red curve in Figure 5A). This may because aptamer-PSA binding events enlarged steric hindrance and inhibited the diffusion of ascorbic acid to electrode surface. As PSA concentration increased from 0.001 to 50 ng/mL, the photocurrent intensity gradually reduced. In other words, there was an excellent negative correlation between photocurrent and logarithmic value of PSA concentrations and corresponding regression curve was $-\Delta I=1.441+0.349 lgC_{PSA}$ (ng/mL) (Figure 5B). This proposed PEC sensing platform possessed a linearity (R^2) at 0.991 with a detection limit at 0.00037 ng/mL (S/N=3). Such performance is primarily because rapid photoinduced charges separation and specific biometric events.

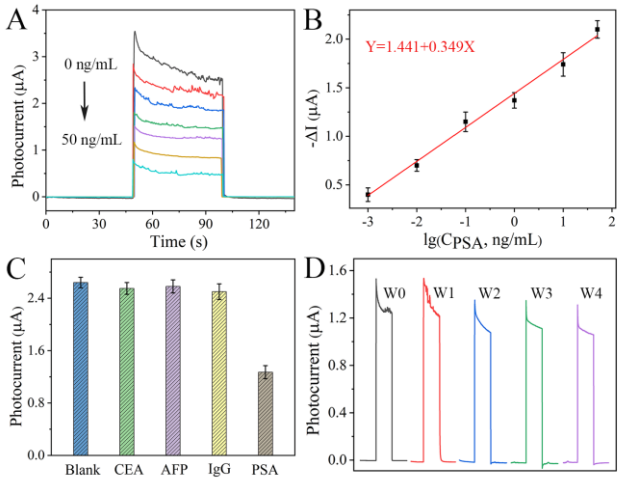

Figure 5. (A) Photocurrent responses of FTO/In_2O_3-$ZnIn_2S_4$/aptamer/BSA at different PSA concentrations (0, 0.001, 0.01, 0.1, 1, 10, 50 ng/mL) and (B) the calibration curve between -ΔI and logarithm of PSA concentration. (C) Photocurrent of proposed biosensing platform in the presence of 1 ng/mL CEA, AFP, IgG, and blank. (D) Photocurrent of PEC biosensor at different storage times from 0 to 4 weeks.

 doi:10.20944/preprints202503.1745.v1

To further assess proposed PEC biosensors, both selectivity and stability were monitored. As illustrated in Figure 5C, significant photocurrent change was only appeared in the presence of 1 ng/mL PSA not other substances including carcinoembryonic antigen (CEA), alpha fetoprotein (AFP), and immunoglobulin G (IgG). This result indicated those interferences had almost no impact on sensing performance. Moreover, the photocurrent response of FTO/In_2O_3-$ZnIn_2S_4$/aptamer/BSA electrodes on 4th week maintained 85% of original value. Results indicated acceptable storage stability.

4. Conclusions

In summary, we successfully constructed an effective PEC biosensor based on FTO/In_2O_3-$ZnIn_2S_4$ sensitization structure and PSA-sensitive aptamer for sensitive analysis of PSA. In_2O_3 tubes were firstly prepared by two-step hydrothermal and annealing methods, followed by the in-situ growth of $ZnIn_2S_4$ nanosheets. In this process, generated tubular composite established efficient energy level matching between In_2O_3 and $ZnIn_2S_4$. This intimate interface contacts inhibited the photocarrier recombination and made effective migration of photoinduced electrons and holes, thus obtaining desirable initial PEC signals. Besides, biological binding sites on hybrid contributed to aptamer-protein event and further achieved PSA sensing. The constructed PEC biosensor. The constructed PEC biosensor presented a wide detection range from 0.001 to 50 ng/mL, with a detection limit down to 0.00037 ng/mL. Developed PEC sensing platform has high sensitivity, satisfying selectivity and stability, and guide the optimal PEC electrode construction for PSA detection.

Supplementary Materials: The following supporting information can be downloaded at the website of this paper posted on Preprints.org, experimental section (reagents and apparatus); Figure S1: Enlarged SEM image of ZnIn2S4.

Author Contributions: H.S.: Conceptualization, methodology, and writing-original draft. J. X.: data curation, investigation, and validation. Y.W.: Funding acquisition, formal analysis, writing-reviewing and editing. All authors have read and agreed to the published version of the manuscript.

Funding: Please add: This research was funded by the Excellent Youth Innovation Team in Universities of Shandong (2022KJ133), and the Science, Education and Industry Integration Innovation Pilot Project from Qilu University of Technology (Shandong Academy of Sciences) (2024RCKY025)..

Data Availability Statement: Data will be made available upon request from the corresponding author.

Conflicts of Interest: The authors declare no conflicts of interest.

References

1. Homer, M. K.; Kuo, D. Y.; Dou, F. Y.; Cossairt, B. M., Photoinduced charge transfer from quantum dots measured by cyclic voltammetry. J. Am. Chem. Soc. 2022, 144, 14226-14234.
2. Qin, Y.; Zhang, J.; Tan, R.; Wu, Z.; Liu, M.; Li, J.; Xu, M.; Gu, W.; Zhu, C.; Hu, L., Small-molecule probe-induced in situ-sensitized photoelectrochemical biosensor for monitoring α-Glucosidase activity. ACS sensors 2023, 8, 3257-3263.
3. Ding, H.; Feng, Y.; Xu, Y.; Xue, X.; Feng, R.; Yan, T.; Yan, L.; Wei, Q., Self-powered photoelectrochemical aptasensor based on MIL-68(In) derived In_2O_3 hollow nanotubes and Ag doped ZnIn2S4 quantum dots for oxytetracycline detection. Talanta 2022, 240, 123153.
4. Nam, B.; Ko, T.-K.; Hyun, S.-K.; Lee, C., NO_2 sensing properties of WO_3-decorated In_2O_3 nanorods and In_2O_3-decorated WO_3 nanorods. Nano Convergence 2019, 6, 40.
5. Zhao, F.; Cao, W.; Wang, P.-H.; Wang, J.; Yu, L.; Qiao, Z.; Ding, Z.-J., Fast and sensitive detection of CO by Bi-MOF-derived porous In_2O_3/Fe_2O_3 core-shell nanotubes. ACS sensors 2023, 8 (12), 4577-4586.
6. Han, C.; Zhang, X.; Huang, S.; Hu, Y.; Yang, Z.; Li, T. T.; Li, Q.; Qian, J., MOF-on-MOF-derived hollow Co_3O_4/In_2O_3 nanostructure for efficient photocatalytic CO_2 reduction. Adv. Sci. 2023, 10, 2300797.

 doi:10.20944/preprints202503.1745.v1

7. Shi, L.; Benetti, D.; Wei, Q.; Rosei, F., MOF-derived In_2O_3/CuO p-n heterojunction photoanode incorporating graphene nanoribbons for solar hydrogen generation. Small 2023, 19, 2300606.
8. Cao, Y.; Lu, K.; Chen, Y.; Zheng, Q.; Huang, C.; Jia, N., In_2O_3/Bi_2S_3 S-scheme heterojunction-driven molecularly imprinted photoelectrochemical sensor for ultrasensitive detection of dlorfenicol. ACS Appl. Mater. Interfaces 2023, 15, 58397-58405.
9. Han C.; Zhang X.; Huang S.; Hu Y.; Yang Z.; Li T.; Li Q.; Qian J., MOF-on-MOF-derived hollow Co_3O_4/In_2O_3 nanostructure for efficient photocatalytic CO_2 reduction. Adv. Sci. 2023, 10 2300797.
10. Liu, X.; Zhang L.; Li Y.; Xu X.; Du Y.; Jiang Y.; Lin K., A novel heterostructure coupling MOF-derived fluffy porous indium oxide with g-C_3N_4 for enhanced photocatalytic activity, Mater. Res. Bull. 2021, 133, 111078.
11. Ren J.; Yuan K.; Wu K.; Zhou L.; Zhang Y., A robust CdS/In_2O_3 hierarchical heterostructure derived from a metal–organic framework for efficient visible-light photocatalytic hydrogen production, Inorg. Chem. Front. 2019, 6, 366–375.
12. Yang, J.; Zhu, X.; Yu, Q.; He, M.; Zhang, W.; Mo, Z.; Yuan, J.; She, Y.; Xu, H.; Li, H., Multidimensional In_2O_3/In_2S_3 heterojunction with lattice distortion for CO_2 photoconversion. Chinese J. Catal. 2022, 43, 1286-1294.
13. Luo, D.; Peng, L.; Wang, Y.; Lu, X.; Yang, C.; Xu, X.; Huang, Y.; Ni, Y., Highly efficient photocatalytic water splitting utilizing a WO_3-x/$ZnIn_2S_4$ ultrathin nanosheet Z-scheme catalyst. J. Mater. Chem. A 2021, 9, 908-914.
14. Ding, S.; Medic, I.; Steinfeldt, N.; Dong, T.; Voelzer, T.; Haida, S.; Rabeah, J.; Hu, J.; Strunk, J., Ultrathin defective nanosheet subunit $ZnIn_2S_4$ hollow nanoflowers for efficient photocatalytic hydrogen evolution. Small Struct. 2023, 4, 2300091.
15. Lu, P.; Liu, K.; Liu, Y.; Ji, Z.; Wang, X.; Hui, B.; Zhu, Y.; Yang, D.; Jiang, L., Heterostructure with tightly-bound interface between In_2O_3 hollow fiber and $ZnIn_2S_4$ nanosheet toward efficient visible light driven hydrogen evolution. Appl. Catal. B Environ. 2024, 345, 123697.
16. Wang, J.; Sun, S.; Zhou, R.; Li, Y.; He, Z.; Ding, H.; Chen, D.; Ao, W., A review: Synthesis, modification and photocatalytic applications of $ZnIn_2S_4$. J. Mater. Sci. Technol. 2021, 78, 1-19.
17. Lin, Y.; Fang, W.; Xv, R.; Fu, L., TiO_2 nanoparticles modified with $ZnIn_2S_4$ nanosheets and Co-Pi groups: Type II heterojunction and cocatalysts coexisted photoanode for efficient photoelectrochemical water splitting. Int. J. Hydrogen Energ. 2022, 47, 33361-33373.
18. Liu, M., Xiong, J., Kong, D., Liu, Y., Wu, H., Li, F., Hu, H.; Wang, D.; Guo, X.; Jiao, Y.; Zhang, Z., Anchoring $ZnIn_2S_4$ nanosheets on oxygen-vacancy NiMoOx nanorods for efficient photocatalytic hydrogen evolution. Sep. Purif. Technol. 2025, 359, 130608.
19. Kong, D.; Hu, X.; Geng, J.; Zhao, Y.; Fan, D.; Lu, Y., Geng, W.; Zhang, D.; Liu, J.; Li, H.; Pu, X., Growing $ZnIn_2S_4$ nanosheets on $FeWO_4$ flowers with pn heterojunction structure for efficient photocatalytic H_2 production. Appl. Surf. Sci. 2022, 591, 153256.
20. Wang, M.; Zhang, G.; Guan, Z.; Yang, J.; Li, Q., Spatially separating redox centers and photothermal effect synergistically boosting the photocatalytic hydrogen evolution of $ZnIn_2S_4$ nanosheets. Small, 2021, 17, 2006952.
21. Liu, T.; Shen, H.; Wang, M.; Feng, Q.; Chen, L.; Wang, W.; Zhang, J., Fabrication of ZnIn2S4 nanosheets decorated hollow CdS nanostructure for efficient photocatalytic H_2-evolution and antibiotic removal performance. Sep. Purif. Technol. 2023, 315, 123698.
22. Wang, S.; Guan, B. Y.; Lou, X. W. D., Construction of $ZnIn_2S_4$-In_2O_3 hierarchical tubular heterostructures for efficient CO_2 photoreduction. J. Am. Chem. Soc. 2018, 140, 5037-5040.
23. Chang, Y.-S.; Choi, M.; Baek, M.; Hsieh, P.-Y.; Yong, K.; Hsu, Y.-J., CdS/CdSe co-sensitized brookite H:TiO_2 nanostructures: Charge carrier dynamics and photoelectrochemical hydrogen generation. Appl. Catal. B Environ. 2018, 225, 379-385.
24. Lu, P.; Liu, K.; Liu, Y.; Ji, Z.; Wang, X.; Hui, B.; Zhu, Y.; Yang, D.; Jiang, L., Heterostructure with tightly-bound interface between In_2O_3 hollow fiber and $ZnIn_2S_4$ nanosheet toward efficient visible light driven hydrogen evolution. Appl. Catal. B Environ. 2024, 345, 123697.

 doi:10.20944/preprints202503.1745.v1